Thermoacoustic range verification in the presence of acoustic heterogeneity and soundspeed errors – Robustness relative to ultrasound image of underlying anatomy

Sarah K. Patch[a)]
Department of Physics, UW-Milwaukee, PO Box 413, Milwaukee, WI 53201, USA

Daniel Santiago-Gonzalez and Brahim Mustapha
Physics Division, Argonne National Laboratory, Argonne, IL 60439, USA

(Received 22 July 2018; revised 11 September 2018; accepted for publication 12 October 2018; published 23 November 2018)

Purpose: To demonstrate robustness of thermooacoustic range verification to acoustic heterogeneity and discrepancies between assumed and true propagation speed, i.e., soundspeed errors.
Methods: A beam sweeper was used to deliver 250 ns pulses that deposited 0.26 Gy of 16 MeV protons and 2.3 Gy of 60 MeV helium ions into water and oil targets, respectively. Thermoacoustic signals were detected by a 96-channel ultrasound array with a 1–4 MHz sensitivity band (−6 dB), bandpass filtered and backprojected to create thermoacoustic images in the plane of the ultrasound array. The same soundspeed and transducer array were used to estimate range and generate the ultrasound images onto which Bragg peak locations were overlaid. An air-gap phantom that displaced the Bragg peak by 6.5 mm demonstrated accuracy. Robustness to soundspeed errors was demonstrated in a waterbath as the assumed propagation speed scanner setting was altered by ±5%. Tissue-mimicking gelatin and a bone sample were introduced to demonstrate robustness to acoustic heterogeneity relative to ultrasound images of the underlying morphology.
Results: Single ion pulse measurements sufficed during the helium run, but signal averaging was required for protons. Range and entry point into the target were estimated from data collected by transducers placed at least 6 cm distal to the Bragg peak. When ultrasound images depicted the air–target interface where the beam enters, estimates of the entry point agreed with ultrasound images and range estimates agreed with Monte Carlo simulations to within 300 μm, even when thermoacoustic emissions traveled through a strongly scattering bone sample. Estimated Bragg peak locations were translated 6.5 mm by the air-gap phantom and correctly identified scenarios when the beam stopped inside the bone.
Conclusions: Soundspeed errors dilate and acoustic heterogeneities deform ultrasound images. When thermoacoustic receivers are co-located with the ultrasound imaging array, the same transformations shift thermoacoustic range estimates. Therefore, thermoacoustic range verification is robust relative to ultrasound images of underlying anatomy. When the treatment target is visible in ultrasound, e.g., prostate, online thermoacoustic range estimates could verify that the treatment spot is inside the target. [https://doi.org/10.1002/mp.13256]

Key words: adaptive planning, IGRT, ion therapy, proton therapy, range verification

1. INTRODUCTION

Range verification is currently the weak link in ion therapy. Current range verification techniques such as prompt gamma, positron emission tomography (PET), and cone beam computerized tomography (CBCT) lack direct correlation to live images of underlying anatomy. PET and CBCT expose organs at risk (OARs) to ionizing radiation. The primary benefit of ion therapy is to spare OARs, but exposure due to CBCT is non-negligible. CBCT improves alignment accuracy over x-ray radiography, but CBCT dose is O(1 mGy) and O(1 cGy) for head and abdominal scans, respectively. OARs in the abdomen can be exposed to one tenth of a Gray from bi-weekly CBCT imaging.

Thermoacoustics could provide online range verification with direct correlation to underlying morphology as depicted in ultrasound images (Fig. 1), without exposing OARs to ionizing radiation. However, thermoacoustic range estimates are skewed by acoustic heterogeneities, and by assuming an incorrect soundspeed. Incorrect soundspeed settings and acoustic heterogeneities dilate and deform ultrasound images, respectively. We demonstrate that thermoacoustic estimates of the Bragg peak location [Fig. 1(b)] are subject to the same transformations as ultrasound images when thermoacoustic receivers are co-located with ultrasound imaging arrays.

Thermoacoustic signals were detected in national laboratories[1,2] and proposed for range verification during particle therapy[3,4] decades ago. Synchrocyclotrons deliver stress-confined pulses that may enable thermoacoustic range verification,[5] as well as future pulsed therapy linacs.[6] A resurgence

generating too many papers to cite is described in recent reviews[7,8] leading to questions about clinical implementation.

A linear array was used to generate ultrasound images that were co-registered to images reconstructed from thermoacoustic emissions measured by a curved array, requiring digital co-registration.[9] To our knowledge, our previous work[10] is the only one that provides inherent co-registration of thermoacoustic range estimates with ultrasound images of underlying anatomy, by using the same ultrasound array to detect thermoacoustic emissions and generate ultrasound images. Thermoacoustic emissions in this report were tailored to the ultrasound array's frequency band, reducing the required dose by three orders of magnitude. 2.3 Gy produced thermoacoustic emissions in Fig. 1(a) from which accurate range estimates were generated. Additionally, in this work we estimate Bragg peak locations from thermoacoustic emissions that traveled through [Fig. 1(c)] and out of a strongly scattering bone sample. Finally, we demonstrate robustness and accuracy of thermoacoustic range estimates relative to ultrasound images with fields of view exceeding 60 mm, despite acoustic heterogeneity and incorrect soundspeed settings on the scanner.

2. MATERIALS AND METHODS

Experiments were performed at the ATLAS facility of Argonne National Laboratory.[11] A series of 12-MHz superconducting resonators accelerated proton and helium-4 (4He) ions for two different experiments. Data were acquired on a programmable ultrasound system using different soundspeed settings. Homogeneous and heterogeneous targets were used to demonstrate robustness relative to ultrasound images, despite soundspeed errors and acoustic heterogeneity.

2.A. Beam specifications

In the first experiment, a 4He beam was accelerated to 60.7 ± 0.4 MeV. In the second experiment, a proton beam with energy of 15.99 ± 0.15 MeV was delivered. The velocity of the 4He beam was measured with the ATLAS time-of-flight (TOF) device, a series of sensors at fixed positions that detect the induced charge from the beam particles. Once the velocity is measured, the energy is computed from the known mass-to-charge ratio of the beam particles. This is the standard approach at ATLAS for determining the beam energy. During the proton run, the TOF device was unavailable; however, the energy of the proton beam was measured with a surface barrier Silicon detector previously calibrated with the TOF device.

Both proton and 4He beams exited the beam line through a 25 μm titanium foil and entered liquid targets through 60 μm acrylic packing tape (Staples). 4He ions and protons traveled through 2 and 19 cm of air between exit foil and the target, respectively. Horizontal and vertical beam cross-sections were asymmetric, as measured using beam profile monitors located 26" upstream of the targets. The 4He beam was focused with full width at half maximum (FWHM) less than 7 mm. At time of writing, exact calibrations for the beam profile monitors are unavailable, but even in the worst case the proton beam was more tightly focused with FWHM less than 3.5 mm (Table I).

A beam sweeper allowed 3 of 120,000 RF cycles to pass to the target at a pulse repetition frequency of 100 Hz. Ion pulse duration was confirmed using a photomultiplier tube with fast plastic scintillator placed below and behind the targets during proton and 4He runs, respectively. A logic signal (TTL) from the sweeper triggered both the oscilloscope (Tektronix DPO7104) and ultrasound system (Verasonics, V1). The time delay between sweeper trigger and PMT signals was used to compute the time at which ions were delivered to the target, which is essential to backproject thermoacoustic signals accurately. During the proton run, trigger and PMT signals were both transmitted from the target room to oscilloscope via coaxial cables of the same length and transmission times, so the 1.3 μs time delay shown on the oscilloscope [Fig. 2(a)] was used to compute range estimates. The 4He beam was accelerated to slightly lower energy per nucleon and was extracted further downstream than the proton beam,

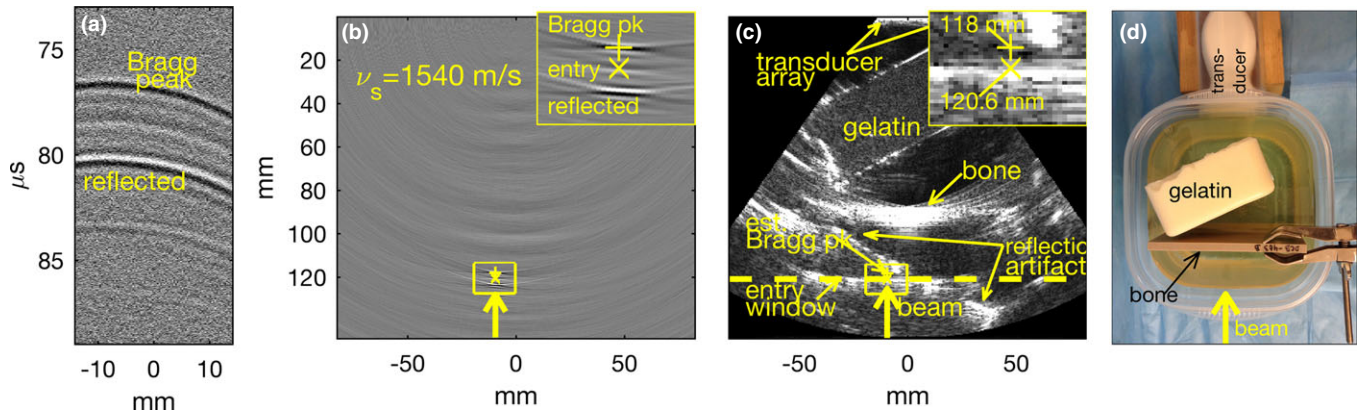

FIG. 1. Thermoacoustic range verification despite acoustic heterogeneity. Thermoacoustic emissions from a single 4He pulse (a) and thermoacoustic image (b) from which Bragg peak location, range, and beam entry point are estimated. (c) Ultrasound image of acoustic scatterers in an oil target with thermoacoustic estimates overlaid. Bragg peak and ion entry locations are overlaid as "+" and "x". Estimated beam entry window plotted in dashed yellow. (d) Aerial photo depicting the experimental setup. [Color figure can be viewed at wileyonlinelibrary.com]

TABLE I. Beam, target, and signal averaging specifications.

Beam	Ave. current (pA)	Lateral FWHM upper bounds (horiz/vert mm)	Ion target	Phantom	FOV (cm)	# aves
Proton	48	2.3/1.7	Water	Air-gap	6	128
		3.5/1.7		Gel and bone	6	128
He	165	3.9/6.9	Water	None	12	1
			Oil	Gel and bone	12	1

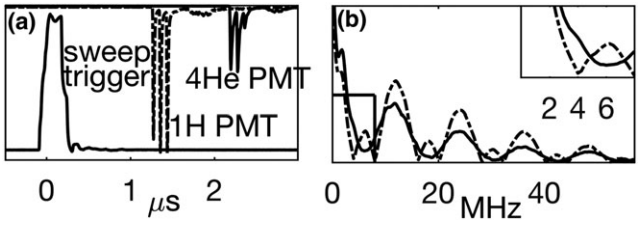

FIG. 2. Trigger and PMT traces from 4He and proton runs in time (a) and frequency (b) domains. PMT traces for protons and helium-4 plotted in dashed and solid, respectively.

so 4He ions arrived later with respect to the sweeper. During the 4He run the cables transmitting the PMT and TTL signals were substantially different in length, which additionally increased the time delay shown on the oscilloscope to 2.2 μs. We empirically determined the true time delay between arrival of the trigger signal and 4He ions to be 1.8 μs based upon thermoacoustic image quality.

The PMT detected O(10) gammas per ion pulse delivered to the target, so pulses were averaged on the scope to generate smooth pulse profiles in Fig. 2(a). (512 and 1024 PMT pulses were averaged for protons and 4He, respectively.) Phase error of the sweeper during the 4He run resulted in severe truncation of the third bunch, which smoothed the spectra of the pulse envelope, but also increased essential bandwidth from 4 MHz = 1/250 ns (proton) to 6 MHz = 1/167 ns (4He), as shown in the inset in Fig. 2(b).

2.B. Targets/phantoms

Water and safflower oil were the background fluids during the proton and 4He runs, respectively. Water has the advantages of extremely low acoustic attenuation and well-known physical properties, whereas safflower oil has the advantage of more realistic acoustic attenuation and approximately three-fold higher specific heat capacity, which leads to more efficient thermoacoustic signal generation. Tissue-mimicking gelatin and bone samples were diffuse and strong acoustic scatterers. Target materials and properties are listed in Table II. In this work, ion beams stop centimeters proximal to the gelatin (Fig. 1) so the Grueneisen is not applicable ("NA"). Additionally, the Grueneisen is unknown for the bone sample.

To optimize acoustic coupling during the proton run, the ultrasound array was mounted in a water-tight fixture on the distal wall of the test tank, approximately 6 cm from the Bragg peak. During the 4He run, acoustic coupling gel (Aquasonic) and an acoustic window of acrylic packing tape coupled the transducer to 0.5 L of oil in a 12 × 12 × 5 cm plastic container.

TABLE II. Target materials and properties.

Material	v_s(mm/μs)	D (mm)	ρ (g/cc)	Z (MRayls)	Γ
Water	1.48	Var	1.00	1.48	0.1
Safflower oil	1.47	Var	0.9	1.32	0.7
Cortical bone	3.17	5.0	1.92	6.09	Unknown
TM gelatin	1.5	35	1.0	1.5	NA

2.B.1. Water

Room temperature, deionized water was used as the first target for both runs to determine the number of pulses required to achieve acceptable signal to noise ratio. Single 4He bunches generated detectable signal in room temperature deionized water and accurate range estimates in oil, whereas 128 proton bunches were required for accurate range estimation in water targets.

2.B.2. Water with air-gap phantom

An aluminum phantom was machined to a thickness of 6.5 mm, and the 60 μm packing tape sealed a 4 cm diameter hole on each end. To vary the beam range within the water-filled tank, the phantom was suspended below a stepper motor (Haydon-Kerk DCM-8028), with translation range of 10 cm. A counterweight was added to ensure that the phantom stayed nearly flush to the entry port during translation. Nevertheless, protons traversed approximately 1 mm of water between entry port and phantom.

2.B.3. Water with TM gelatin and 5 mm cortical bone

Two objects were used to introduce acoustic heterogeneity: tissue-mimicking gelatin[12] prepared in our laboratory and a commercial 5 mm thick bone sample (CIRS #DCB-403B). Again, the bone mimicking sample was positioned nearly flush with the tape through which protons entered the water. Soundspeed was estimated at the center and four corners of the cortical bone sample using a 5.0 MHz single element transducer (Olympus C310) pulser-receiver (Olympus 5900PR). Sample thickness was measured using a micrometer at the corners and averaged to confirm 5.0 mm sample thickness. Five pulse echoes were created by propagating through room temperature deionized water toward the center and each of the four corners. Time-of-flight through the bone sample was estimated using a standard technique that is described in detail below and referenced in Sections 2.E.3 and 3.B.

For each pulse echo two time series were created and then correlated to determine the temporal lag between the initial echo from the proximal water–bone interface and subsequent echo from the distal bone–water interface. The first time series contained only the initial echo from the proximal water–bone interface, by nulling all values for which $t_{Pk} + 1.5\,\mu s < t$, where t_{Pk} represents the time at which the pulse echo achieved its maximum amplitude. The second time series contained subsequent echoes by nulling all values for $t < t_{Pk} + 1.5\,\mu s$. These time series were correlated via FFT. The point at which the correlated time series achieved its maximum absolute value was taken as the time shift between echoes from the proximal and distal walls of the bone sample. Dividing the 5 mm thickness by half of the time shift yielded a propagation speed of 3.17 ± 0.01 mm/μs.

2.B.4. Oil with TM gelatin and 5 mm cortical bone

The 5 mm cortical bone sample was placed approximately 4 cm distal to the beam entry point so the beam stopped in oil, rather than in the bone sample. Thermoacoustic emissions traveled through the oil, bone sample and a 35 mm thick layer of tissue-mimicking gelatin containing diffuse acoustic scatterers before reaching the ultrasound array. As viewed in the ultrasound imaging plane the entry tape and bone sample were positioned parallel to the array, whereas the gelatin was rotated approximately 45-degrees, (Fig. 1).

2.C. Monte Carlo Simulations

Monte Carlo simulations were performed to model the energy deposited by stopping ion because induced pressure is proportional to energy density, $\Delta p = \Gamma E/V = \Gamma \rho D$ where Γ is the dimensionless Grueneisen, ρ is density, and D is dose in Gy. Stoichiometry for the bone sample was provided by CIRS, Inc. and input into a custom library in Transport and Range of Ions in Material (TRIM) software for layered targets. Stoichiometry for safflower oil was unavailable, so stoichiometry for olive oil was computed from three different sources, all of which were imported into the custom library and yielded similar results. TRIM's compound dictionary was used to model air-gaps, water, and acrylic tape. Air and water values were imported from the nuclear physics materials category and values for "plexiglass, acrylic" were imported from the plastics/polymers category. TRIM simulations using stopping power from SRIM-2008[13] were run with 99k ions traveling perpendicular to the titanium entry foil, with initial positions and energies distributed to mimic the experimental values in Table I. Ion position and energy were written to a file every 100 eV. A custom MATLAB script read in the positions and energies and computed the energy density deposited on a grid with anisotropic resolution: Δz = 10 μm, whereas $\Delta x = \Delta y = 100\,\mu m$ in the longitudinal and lateral directions, respectively. Energy density along the center 5 mm diameter of the beam was computed.

Target layers are listed in Table III, along with location of the Bragg peak, FWHM and distal half-width-at-tenth-maxima (HWTM) of the Bragg curve, and beam energy. In all cases, the boundary between layers 2 and 3 is a strong acoustic reflector. Therefore, thicknesses of layers 1–2 are subtracted from the Bragg peak depth to determine the beam range in the thermoacoustic target. The water layer thickness proximal to the air-gap and bone phantoms was adjusted to match observed arrival times, and in both cases was found to be 1 mm.

2.D. Acoustic hardware

Data were acquired by a 96-channel ultrasound array with 6 dB bandwidth of 1–4 MHz (ATL, P4-1) attached to a programmable ultrasound system (Verasonics V1). The V1 and host computer were positioned several feet below the ion beam. The ultrasound array was placed on the beam trajectory, distal to the Bragg peak. 100′ VGA and USB cables connected the host computer to peripherals (monitor, keyboard,

TABLE III. Target layers and depths for TRIM simulations.

Layer #	Water	Bone	Air-gap	Safflower oil
1	25 μm Ti	25 μm Ti	25 μm Ti	25 μm Ti
2	19 cm air	19 cm air	19 cm air	2 cm air
3	60 μm acrylic	60 μm acrylic	60 μm acrylic	60 μm acrylic
4	3 mm water	1 mm water	1 mm water	3 mm oil
5		5 mm bone	60 μm acrylic	
6			6.5 mm air	
7			60 μm acrylic	
8			2 mm water	
TRIM target depth	193.085 mm	196.085 mm	199.705 mm	23.085 mm
Acoustic target entry	190.025 mm	190.025 mm	190.025 mm	20.025 mm
TRIM Bragg pk depth	192.49 mm	191.96 mm	198.97 mm	22.54 mm
TRIM Range in target	2.47 mm	1.94 mm	8.95 mm	2.51 mm
Bragg curve FWHM	390 μm	240 μm	390 μm	230 μm
Distal HWTM	160 μm	90 μm	160 μm	80 μm
Beam energy	16.0 ± 0.15 MeV	16.0 ± 0.15 MeV	16.0 ± 0.15 MeV	60.7 ± 0.4 MeV

and mouse) located outside the vault. Data acquisition was triggered by the logic signal shown in Fig. 2(a), which was split, with one line to V1 and other to the oscilloscope located outside.

2.E. Software

2.E.1. Data acquisition

Thermoacoustic signal was acquired using custom Matlab scripts. During the 4He run, ultrasound images were first acquired using the vendor-supplied "WideBeam" script that utilized 2.5 MHz ultrasound pulse echoes and stored to disc in a ".mat" file. A Matlab script written to acquire thermoacoustic data[5] was modified to call data processing scripts that overlaid range estimates onto the ultrasound images. For the proton run, the data acquisition script was rewritten to interleave acquisition and processing of ultrasound and thermoacoustic signals. Interleaving ultrasound and thermoacoustic data acquisition provides the advantage of online co-registration, but currently we are capable of programming only one set of data acquisition parameters. Settings were optimized for thermoacoustics at the expense of ultrasound image quality. For instance, signal was acquired with maximum gain settings on the V1 GUI.

2.E.2. Reconstruction and display

Assuming instantaneous deposition and ideal point detectors, exact reconstruction of the thermoacoustic pressure jump can be achieved by applying a first order differential operator and backprojecting, or integrating over a two-dimensional measurement aperture surrounding the region of interest.[14,15] Results below provide limited angle reconstructions since we only have access to measurements over the 3 cm linear aperture of the ultrasound array. Frequency response of the P4-1 array is specified to drop by 6 dB at either end of the 1–4 MHz sensitivity band, compared to peak sensitivity near 2.5 MHz. Previously, we demonstrated that software filtering by application of the Hilbert transform combined with hardware filtering of 2.25 MHz single element transducers (Olympus V306) and preamplifiers (Olympus 5662) effectively mimics a temporal derivative.[16] We have found that the Verasonics V1 data acquisition chain effectively applies a Hilbert transform, so data are backprojected after application of a bandpass filter.

Data processing was modified from our previous work[10] to overlay the Bragg peak location during thermoacoustic data acquisition, rather than offline. During the proton run, the ultrasound image was updated for each new thermoacoustic range estimate. Additional software modifications included 2× upsampling thermoacoustic data in time prior to one-way beamforming onto an image lattice that was 4× upsampled in the longitudinal direction relative to the ultrasound image and providing estimates of the beam entry depth in addition to the Bragg peak location.

2.E.3. Validation/consistency checks

Two consistency checks were applied to our results. First, thermoacoustic range estimates were compared to Monte Carlo simulations. Second, the beam entry position was estimated from thermoacoustic images and then compared to ultrasound images that visualize the beam entry window.

Thermoacoustic signals generated in homogeneous targets often have a characteristic "3-stripe" signature [Fig. 1(a)]. The first stripe emanates from the Bragg peak and travels directly to the receiver. The second stripe emanates from the beam entry point, has opposite polarity to the first stripe and travels directly to the receiver. The third stripe emanates from the Bragg peak, reflects off the entry window and travels to the receiver with polarization unchanged. The stripes manifest themselves in thermoacoustic images as three marks separated in the depth direction by the beam range into the target [Fig. 1(b)]. Therefore, range estimates were based upon direct and reflected thermoacoustic signals from the Bragg peak, by applying to thermoacoustic images a two-dimensional version of the technique described in Section 2.B.3 to estimate soundspeed in the bone sample from ultrasound time series. Details are provided in the Supporting Information Data S1.

Range was added to the depth of the Bragg peak location to estimate where the beam entered the target. Although Bragg peak locations cannot be seen in ultrasound images, the entry depth into the target is almost always visible because interfaces between materials of different stopping power typically cause acoustic reflections. Therefore, accuracy of beam entry depth estimates derived from thermoacoustic images were validated relative to the ultrasound images.

3. RESULTS

The results presented below were computed offline for averages of 128 thermoacoustic emissions, ultrasound image quality was optimized, and color annotations were added but are otherwise similar to results computed online from averages of 256 emissions.

3.A. Protons into water with air-gap phantom to translate Bragg peak

Data acquisition commenced using Verasonics' default soundspeed setting of 1540 m/s in Figs. 3(a)–3(c). The soundspeed setting was then reduced to 1480 m/s to match that of water in Figs. 3(d)–3(i). Estimated Bragg peak locations are indicated by yellow "+" and entry points by "x." Note that the time series in Figs. 3(a) and 3(c) remained essentially unchanged, while the thermoacoustic estimates and ultrasound images (d) contracted compared to (b). Then, a 6.5 mm air-gap was introduced within approximately 1 mm of the entry tape. Thermoacoustic emissions arrived earlier and were not as well separated (e) because the air-gap phantom was not perfectly flush with the entry wall. Protons

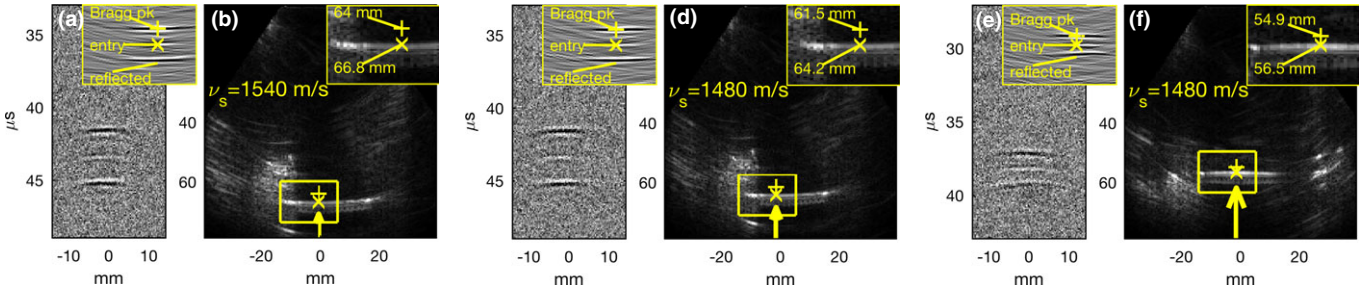

FIG. 3. Thermoacoustic time series, backprojected data, and ultrasound images with overlays of Bragg peak locations (+) and corroborating entry point estimates (x). Vertical arrows indicate proton beam direction. (a–b) No air-gap, $v_s = 1.54\,\text{mm}/\mu\text{s}$. (c–d) No air-gap, $v_s = 1.48\,\text{mm}/\mu\text{s}$. (e–f) 6.5 mm air-gap, $v_s = 1.48\text{mm}/\mu\text{s}$. [Color figure can be viewed at wileyonlinelibrary.com]

traveled some distance in water before encountering the air-gap, that reduced their range after exiting the air-gap. Nevertheless, the estimate of the Bragg peak location shifted by 6.6 mm, from 61.5 mm in subfigure (d) to 54.9 mm in subfigure (f). As shown in the insets in Figs. 3(b) and 3(d), range into the water target was estimated to be 2.8 and 2.7 mm for $v_s = 1540\,\text{m/s}$ and $v_s = 1480\,\text{m/s}$, respectively. Additionally, all thermoacoustic estimates of the proton beam entry depth are consistent with the ultrasound images.

Using a soundspeed of 1480 m/s yields thermoacoustic range estimates that agree with Monte Carlo results to within 300 microns. TRIM Monte Carlo simulations predict ranges of 2.47 and 8.95 mm without and with the air-gap phantom, respectively. The initial thermoacoustic range estimate into water of 2.8 mm = 66.8 − 64 mm in Fig. 3(c) was generated assuming a soundspeed of 1540 m/s. Reducing the scanner's soundspeed setting to 1480 m/s contracted both ultrasound and thermoacoustic images, shifting the location of the beam entry point and reducing the range estimate to 2.7 mm = 64.2 − 61.5 mm. Introducing a 6.5 mm air-gap within the beamline shifted TRIM and experimental estimates of the Bragg peak location by 6.5 and 6.6 mm, respectively.

Average beam currents in Table I and 100 Hz repetition rate imply approximately 3 M protons per pulse. Taking the per proton dose at the Bragg peak of 0.85e-7 Gy from Fig. 4 implies a per pulse dose of 0.26 Gy at the Bragg peak. Online

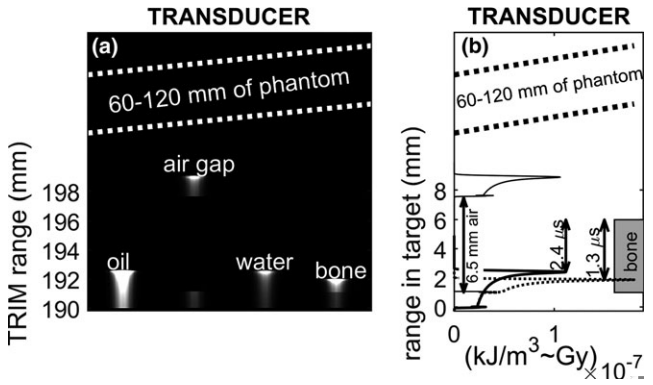

FIG. 4. TRIM simulation results. (a) cross-sections of dose maps. (b) Per proton energy density along central 5 mm diameter cylinder along the beam axis in water target (thin), 6.5 mm air-gap phantom (thick dashed), and bone (thin dashed). Energy density in oil not plotted.

estimation of beam range and Bragg peak location was computed by averaging signals from 256 pulses, which delivered a total dose of 66 Gy for all protons into water experiments.

Rudimentary repeatability testing was performed by acquiring several 256 pulse realizations for each soundspeed setting and phantom configuration. Each individual thermoacoustic emission was saved to disk, and 128 pulses (33 Gy) were sufficient during offline analysis with optimized software. Each 256-pulse dataset was broken into two 128-pulse datasets to generate mean and standard deviations of Bragg peak coordinates and beam range in Table IV.

When soundspeed was taken to be 1540 m/s, range estimates between the no air-gap and no bone experiments agreed well: 2.79 ± 0.06 vs 2.74 ± 0.13. We attribute differences in z_{pk} estimates (63.97 ± 0.03 vs 63.60 ± 0.00) to repositioning of the ultrasound array between experiments. Estimates of z_{pk} are extremely repeatable in all cases, whereas estimates of $x_{pk}$are not. Finally, range estimates are repeatable only when the beam stops in water.

3.B. Protons into water and cortical bone sample with diffuse acoustic scatterers between Bragg peak and transducer

To demonstrate the effect of heterogeneity in both proton stopping power and soundspeed, the 5 mm thick bone sample

TABLE IV. Repeatability of proton beam estimates generated by averaging 128 individual pulses.

Experiment	v_s (m/s)	N	z_{pk} (mm)	x_{pk} (mm)	Range (mm)
No Air-gap	1540	10	63.97 ± 0.03	−0.18 ± 0.75	2.79 ± 0.06
No Air-gap	1480	8	61.49 ± 0.04	−0.92 ± 0.33	2.65 ± 0.09
6.5 mm air-gap	1480	8	54.90 ± 0.04	−1.21 ± 0.45	1.53 ± 0.12
Bone	1620	6	64.98 ± 0.03	1.08 ± 0.40	1.28 ± 0.92
Bone	1540	10	61.76 ± 0.02	0.41 ± 0.47	1.24 ± 0.68
Bone	1470	8	58.81 ± 0.04	0.52 ± 0.58	1.36 ± 0.61
No Bone	1620	10	66.94 ± 0.04	−0.56 ± 1.17	2.92 ± 0.10
No Bone	1540	6	63.60 ± 0.00	−0.87 ± 0.79	2.74 ± 0.13
No Bone	1470	6	60.56 ± 0.04	0.00 ± 1.02	2.54 ± 0.12

with high propagation speed was positioned so that protons traversed a thin layer of water and stopped inside the bone sample. Ultrasound images were collected using a soundspeed of 1540 m/s to most closely match the propagation speed in muscle mimicking gelatin. Figure 5 compares thermoacoustic emissions and range estimates when the beam stops in the bone sample [5(a), 5(b)] and when it stops in water [5(c), 5(d)]. Comparing Figs. 5(c), 5(d) with Figs. 3(a), 3(b) demonstrates that the diffusely scattering gelatin shifted the ultrasound image and thermoacoustic estimates of the beam entry depth by 400 microns but left the range estimate unchanged at 2.8 mm. When the beam stopped in bone, however, subsequent thermoacoustic signal was garbled due to multiple reflections within the bone and also additional signals from the water–bone interface.

Although the presence of a dense bone sample reduced the proton range and translated the Bragg peak further from the ultrasound transducer, the initial compression pulse due to the Bragg peak in the bone arrived 1 μs earlier than when the target was only water. The time shift was computed by applying the same convolution technique described in Section 2.B.3 to time series from eight channels centered about $x = -1.33$ mm in Figs. 5(a) and 5(c). Early arrival was due to the faster propagation speed in bone compared to water and was consistent with a 1-mm water layer between the entry window and bone, as depicted in Fig. 4, and calculated below.

Consider the acoustic time-of-flight from the Bragg peak to the distal side of the bone sample in the TRIM coordinate system at z = 196.085 mm as depicted in Fig. 5(b). Thermoacoustic pulses traversed 4.13 mm = 196.085 − 191.96 mm through bone which requires only 1.3 μs. In the homogeneous waterbath, the thermoacoustic pulse required more time to traverse a shorter path: a distance of 3.595 mm = 196.085 − 192.49 mm, required 2.4 μs. Therefore, time-of-flight differences should have been 1.1 μs, in agreement with Figs. 5(a) and 5(c).

Comparing thermoacoustic emissions emanating from bone [Fig. 5(a)] and water [Fig. 5(b)], the bone generates a stronger pulse at the Bragg peak, but it obscures the expected signal from the entry point and reflected emissions from the Bragg peak are also obscured due to multiple reflections within the bone sample.

Nevertheless, thermoacoustic range estimates based upon the initial compressional pulse are consistent with the diagnostic portion of the ultrasound image. In Fig. 5(a) the Bragg peak estimate lies within the bone, rather than water, but in subfigure (b) the Bragg peak estimate again lies 2.8 mm inside the tank when soundspeed is assumed to be 1540 m/s. Absolute (room) coordinates for Bragg peak location are incorrect when high-soundspeed bone lies between the Bragg peak and transducer, but the results are accurate relative to the ultrasound image. Utility of thermoacoustic range estimates is diminished when ultrasound image quality breaks down, as at depths beyond the water–bone interface in Fig. 5(b).

3.C. He into oil with TM gelatin and 5 mm bone

In this case the imaging field of view was larger and the bone sample was placed 4 cm distal to the Bragg peak, so 4He ions stopped in safflower oil, mimicking a benchtop example published earlier in which a single element transducer transmitted a pulse to an ultrasound array[17] (Supporting Information).

No signal averaging was required because thermoacoustic pulse amplitudes were higher for multiple reasons: each 4He ion deposited fourfold the energy near the Bragg peak of a proton, more efficient conversion of thermal to mechanical energy in oil ($\Gamma = 0.7$) compared to water ($\Gamma = 0.1$), and higher beam current during the 4He run. Additionally, deposited energy maps differed because relative energy spread for 4He was smaller than for the proton beam (0.6% vs 0.9%), but the proton beam was more tightly focused. TRIM simulations showed that the per ion energy density along the central 1 mm was 3.9e-7 kJ/m^3 for the helium beam, and 5.5 M ions were delivered per pulse. Density of cooking oils is approximately 900 kg/m^3, so the 4He beam delivered approximately 2.3 Gy per pulse.

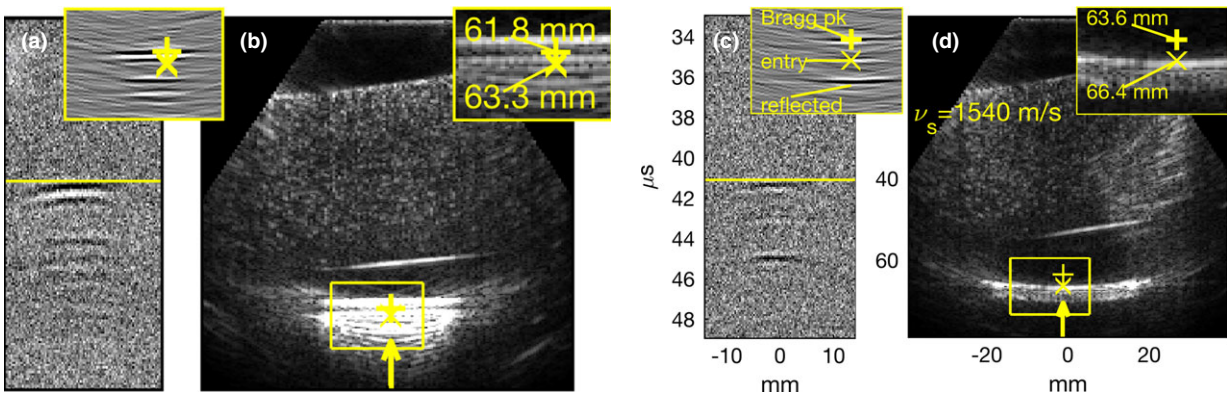

FIG. 5. Thermoacoustic time series, relevant parts of reconstructions, and comparison to ultrasound when the beam stopped in bone (a–b) and water (c–d). To aid comparison of the time series, lines are drawn at 40 μs in Fig. 5(a) and 41.1 μs in Fig. 5(c). Soundspeed set to 1540 m^{-s}.[Color figure can be viewed at wileyonlinelibrary.com]

TABLE V. Estimates for 4He into oil with and without scatterers, assuming $v_s = 1540 m/s$.

Experiment	N	z_{pk} (mm)	x_{pk} (mm)	*range* (mm)	*range* $*$ 1470/1540
Control	7	121.82 ± 0.06	−11.62 ± 0.39	2.89 ± 0.00	2.76
W/bone and gelatin	8	118.10 ± 0.06	−8.78 ± 0.47	2.67 ± 0.13	2.55

The presence of bone and gelatin repeatably shifted the average estimate of the Bragg peak z- and x- locations by 3.7 and 2.8 mm, commensurate with deformation of the ultrasound image. Results are detailed in Table V, where range estimates assumed soundspeed of 1540 m/s, because that was used to create the ultrasound image in Fig. 1. Recomputing the range with the soundspeed of oil reduces range estimates to within 250 microns of the TRIM simulations. Images of one oil-only realization are provided in the Supporting Information Data S2.

4. DISCUSSION

In this work we demonstrated that thermoacoustic range verification is robust *relative to the ultrasound image of underlying anatomy.*

Thermoacoustics may prove a clinically effective and relatively inexpensive range verification technique for the particle therapy market. Incorporating ultrasound systems into ion therapy vaults could provide low-cost, small-footprint, and nonionizing online image-guided therapy. Customized ultrasound systems would be slightly more expensive but could also provide online range verification that is inherently co-registered to the underlying ultrasound image.

When the target volume is inconspicuous in ultrasound images, co-registration to the planning CT will be required and could be performed by existing commercial ultrasound-CT "fusion" products. Ultrasound-CT co-registration is becoming commonplace due to many advantages such as reduced interventional procedure times,[18] the ability to track a moving organ,[19] and improved outcomes for applications such as liver biopsy.[20] Submillimeter errors have been reported after segmenting the planning CT and applying organ specific soundspeed corrections.[21,22] Therefore, thermoacoustic estimates of the Bragg peak location can be transformed into room coordinates along with ultrasound images.

Weaknesses of thermoacoustic range verification are that it is only appropriate for targets that can be imaged by ultrasound and that thermoacoustic emissions have low amplitude. In soft tissue, the factors converting dose into pressure range from approximately 2 Pa/cGy in muscle and organs to 8 Pa/cGy in fat and 15 Pa/cGy in bone.[23] Instantaneous deposition of 2 Gy increases pressure by less than 500 Pa in a tumor. The Grueneisen parameters of water and cooking oil are approximately 0.1 and 0.7 so amplitudes of thermoacoustic emissions were at most $\Gamma\rho D = 0.1 \cdot 0.26\,\text{Gy} \cdot 1000\,\frac{\text{kg}}{\text{m}^3} = 26\,\text{Pa}$ and $0.7 \cdot 2.3\,\text{Gy} \cdot 900\,\frac{\text{kg}}{\text{m}^3} = 1.4\,\text{kPa}$, assuming stress confinement was satisfied.

Failing to satisfy stress confinement reduces signal strength, so to determine whether stress confinement was satisfied we divide the FWHM of Bragg curves by soundspeeds of targets to compute travel times of 260, 160, and 75 ns, in water, oil and bone, respectively. Three full proton bunches were delivered within 200 ns so stress confinement was satisfied when protons stopped in water, but not in bone. The truncated third 4He bunch [Fig. 2(a)] delivered to the oil target reduced ion pulse duration so that stress confinement was again obeyed. At clinical beam energies, straggle broadens the Bragg peak region so that stress confinement is satisfied by pulse durations of several microseconds and synchrocyclotrons are already capable of delivering pulses in less than 10 ms.

This work demonstrates that thermoacoustic range verification may be feasible in the presence of bone and air-gaps. The (amplitude) reflection coefficient between bone and water/soft tissue is approximately R_{bone}~0.6, so thermoacoustic emissions traveled through a bone sample (Fig. 1) with sufficient amplitude to provide accurate range estimates relative to an ultrasound image that visualized the beam entry window. When the beam stopped in bone, thermoacoustic emissions were strong, and accurate relative to the ultrasound depiction of the distal side of the bone sample [Fig. 5(b)], but multiple reflections between the bone-water interfaces and nearby air-target entry window rendered the proximal region of the ultrasound image as nondiagnostic. The reflection coefficient at an air–tissue interface is very nearly one, so air-gaps will limit utility to geometries where the path between the Bragg peak and acoustic receivers is air-free, as in Fig. 3(f).

A weakness of this study is the fact that low beam energies were required to generate thermoacoustic emissions that our current acoustic hardware can detect and overlay onto ultrasound images. Technical difficulties encountered during the 4He run were primarily on the acoustic side: acoustic coupling through acrylic tape introduced losses, and the tape was not perfectly perpendicular to the beam trajectory. Additionally, the safflower oil target was difficult to model accurately in TRIM. Low proton beam current forced us to signal average to improve SNR. Nevertheless, range estimates were obtained by backprojecting (or one-way beamforming) over distances exceeding 60 mm, so 300 μm error represents only 0.5% of the distance between the transducer array and Bragg peak. Furthermore, thermoacoustic estimates of the ion beam's entry point into the target agreed with ultrasound images of the air–target interface, providing confidence in range estimates relative to the underlying ultrasound images. In practice, ultrasound images may not visualize both the Bragg peak location and entry point of high-energy beams with ranges exceeding 15 cm. However, validation for clinical beam energies could be performed in waterbaths because the acoustic attenuation of water is exceedingly low.

Bandwidth of thermaocoustic emissions should be matched to acoustic receivers. Thermoacoustic emissions were tuned to the 1–4 MHz sensitivity band of the ultrasound array for two reasons: Bragg curves of low energy particle beams were sharp and pulse durations were short.

Thermoacoustic emissions due to instantaneous ion delivery are bandlimited by the energy density map which induces a pressure jump within the beam. For transducers placed distal and on the beam trajectory in a water bath, the thermoacoustic signal bandwidth corresponds to the Bragg curve. (Acoustic attenuation in water is nearly zero.) Although full width at half maximum is often used as a proxy for half-wavelength, we consider the half-width-at-tenth-maximum (HWTM) of the curve distal to the Bragg peak. Doubling the HWTM to approximate one wavelength and dividing into soundspeed yields bandwidths of $4.6\,\mathrm{MHz} = \frac{1.48\,\mathrm{mm\,\mu s^{-1}}}{(2\times 160\,\mu\mathrm{m})}$, $8.6\,\mathrm{MHz} = \frac{3.1\,\mathrm{mm\,\mu s^{-1}}}{(2\times 180\,\mu\mathrm{m})}$, and $9.2\,\mathrm{MHz} = \frac{1.47\,\mathrm{mm\,\mu s^{-1}}}{(2\times 80\,\mu\mathrm{m})}$ when the beam stopped in water, bone, and oil, respectively.

In practice, emissions are further bandlimited by the ion pulse envelope[24–26] and measurements are bandlimited by the receive hardware. The 3-bunch proton pulse envelope bandlimited emissions to 4 MHz, whereas the shorter 4He pulse envelope bandlimited to 6 MHz [Fig. 2(b)]. Additionally, measurements were bandlimited to 4 MHz by the P4-1 transducer array. 185 μm half-wavelengths in water and oil provide best-case resolution limits. We achieved agreement of 230 and 250 μm between TRIM and thermoacoustic range estimates in water and oil, respectively.

Range straggle of protons and 4He ions with range exceeding 20 cm bandlimits thermoacoustic emissions below 100 kHz so custom acoustic transducers will be required to detect both low frequency thermoacoustic emissions and generate ultrasound images using pulse echoes with center frequencies exceeding 1 MHz. Fortunately, dispersion is minimal below 1 MHz, so co-registration of range estimates with ultrasound images will remain accurate despite the fact that thermoacoustic and ultrasound signal bandwidths differ by at least one order of magnitude.

Robustness of range estimates to microscopic heterogeneities should improve as wavelength increases, although accuracy of range estimates computed via one-way beamforming will decrease. To overcome the classic diffraction limit associated with inverse source problems, leveraging *a priori* information may be required. One approach is to use Monte Carlo dose maps computed by the treatment planning system (TPS) to simulate noise-free thermoacoustic emissions simulated for each planning beamlet and then compare to noisy measured emissions.[17]

Data,.mp4 videos, and.png images acquired online during data acquisition and also software used to create all images may be obtained by contacting patchs@uwm.edu.

ACKNOWLEDGMENTS

This material is based upon work supported by the U.S. Department of Energy, Office of Science, Office of Nuclear Physics, under contract number DE-AC02-06CH11357. This research used resources of ANL's ATLAS facility, which is a DOE Office of Science User Facility. SKP thanks Ted Lynch of CIRS, Inc. for providing tissue-mimicking samples; A Jackson and W Byrne of LBNL for providing the scintillator/PMT assembly and S Zhu for providing a high voltage power supply; M Condon for fabricating the air-gap phantom; YM Qadadha for creating the custom TRIM library for phantoms; ATLAS operations and J. Nolen for facilitating the experiments.

DISCLOSURES

The authors have no financial conflicts of interest to disclose.

[a]Author to whom correspondence should be addressed. Electronic mail: patchs@uwm.edu; Telephone: 414-229-4475.

REFERENCES

1. Sulak L, Armstrong R, Baranger H, et al. Experimental studies of the acoustic signature of proton beams traversing fluid media. *Nucl Instrum Methods*. 1979;161:203–217.
2. Askariyan GA, Dolgoshein BA, Kalinovsky AN, Mokhov NV. Acoustic detection of high energy particle showers in water. *Nucl Instrum Methods*. 1979;164:267–278.
3. Tada J, Hayakawa Y, Hosono K, Inada T. Time resolved properties of acoustic pulses generated in water and in soft tissue by pulsed proton beam irradiation-A possibility of doses distribution monitoring in proton radiation therapy. *Med Phys*. 1991;18:1100–1104.
4. Hayakawa Y, Tada J, Arai N, et al. Acoustic pulse generated in a patient during treatment by pulsed proton radiation beam. *Radiat Oncol Invest*. 1995;3:42–45.
5. Lehrack S, Assmann W, Bertrand D, et al. Submillimeter ionoacoustic range determination for protons in water at a clinical synchrocyclotron. *Phys Med Biol*. 2017;62:L20.
6. Ostroumov P, Goel B, Mustapha A, et al. Compact Carbon Ion Linac. In: Chicago; 2016. http://accelconf.web.cern.ch/AccelConf/napac2016/papers/moa4co04.pdf.
7. Parodi K. Tracking proton therapy with acoustic waves. February 2018. https://physicsworld.com/a/tracking-proton-therapy-with-acoustic-waves/. Accessed July 1, 2018.
8. Hickling S, Xiang L, Jones KC, et al. Ionizing radiation-induced acoustics for radiotherapy and diagnostic radiology applications. *Med Phys*. 2018;45:e707–e721.
9. Kellnberger S, Assmann W, Lehrack S, et al. Ionoacoustic tomography of the proton Bragg peak in combination with ultrasound and optoacoustic imaging. *Sci Rep*. 2016;6:29305.
10. Patch S, Kireeff-Covo M, Jackson A, et al. Thermoacoustic range verification using a clinical ultrasound array provides perfectly co-registered overlay of the bragg peak onto an ultrasound image. *Phys Med Biol*. 2016;61:5621–5638.
11. Pardo RC, Savard G, Janssens RVF. ATLAS with CARIBU: a laboratory portrait. *Nucl Phys News*. 2016;26:5–11.
12. Lazebnik M, Madsen EL, Frank GR, Hagness SC. Tissue-mimicking phantom materials for narrowband and ultrawideband microwave applications. *Phys Med Biol*. 2005;50:4245–4528.
13. Ziegler J, Ziegler M, Biersack J. SRIM – the stopping and range of ions in matter (2010). *Nucl Instrum Methods Phys Res, Sect B*. 2010;268:1818–1823.
14. Patch SK. Thermoacoustic tomography-consistency conditions and the partial scan problem. *Phys Med Biol*. 2004;49:2305–2315.
15. Xu M, Wang LV. Universal back-projection algorithm for photoacoustic computed tomography. *Phys Rev E*. 2005;71:016706.

16. Eckhart AT, Balmer RT, See WA, Patch SK. Ex vivo thermoacoustic imaging over large fields of view with 108 MHz irradiation. *IEEE Trans Biomed Eng*. 2011;58:2238–2246.
17. Patch SK, Hoff DEM, Webb TB, Sobotka LG, Zhao T. Two-stage ionoacoustic range verification leveraging Monte Carlo and acoustic simulations to stably account for tissue inhomogeneity and accelerator-specific time structure – a simulation study. *Med Phys*. 2018;45:783–793.
18. Ahmed Y, Novak RD, Nakamoto D, Azar N. Is ultrasound fusion a reasonable replacement for computed tomography in guiding abdominal interventions? *J Ultrasound Med*. 2016;35:1131–1141.
19. Omari EA, Erickson B, Ehlers C, et al. Preliminary results on the feasibility of using ultrasound to monitor intrafractional motion during radiation therapy for pancreatic cancer. *Med Phys*. 2016;43:5252.
20. Bo X-W, Xu H-X, Wang D, et al. Fusion imaging of contrast-enhanced ultrasound and contrast-enhanced CT or MRI before radiofrequency ablation for liver cancers. *BJR*. 2016;89:20160379.
21. Fontanarosa D, van der Meer S, Harris E, Verhaegen F. A CT based correction method for speed of sound aberration for ultrasound based image guided radiotherapy. *Med Phys*. 2011;38:2665–2673.
22. Fontanarosa D, van der Meer S, Verhaegen F. On the significance of density-induced speed of sound variations on US-guided radiotherapy. *Med Phys*. 2012;39:6316–6323.
23. Duck F. *Physical Properties of Tissue*. London/San Diego, CA: Academic Press; 1990.
24. John F. *Partial Differential Equations*, 4th ed. New York, NY: Springer; 1981:135–136.
25. Alsanea F, Moskvin V, Stantz KM. Feasibility of RACT for 3D dose measurement and range verification in a water phantom. *Med Phys*. 2015;42:937–946.
26. Jones KC, Seghal CM, Avery S. How proton pulse characteristics influence protoacoustic determination of proton-beam range: simulation studies. *Phys Med Biol*. 2016;61:2213.

SUPPORTING INFORMATION

Additional supporting information may be found online in the Supporting Information section at the end of the article.

Data S1. Range estimation from thermoacoustic images.
Data S2. Additional results.

Supplemental Information

A. Range Estimation from Thermoacoustic Images

Copies of the thermoacoustic image were created and modified as follows: The first contained only the Bragg peak because pixels for all $z > z_{BP} + 1\ mm$ were nulled (Fig. S1a). The second contained only the entry point and reflected Bragg peak signal because pixels corresponding to $z < z_{BP} + 1\ mm$ were nulled (Fig. S1b). These images were correlated via 2D FFT (Fig. S1c), the maximum was selected and the corresponding shift in the depth direction was divided by two to estimate beam range into the target. Adding the range to z_{BP} provided an estimate of the entry depth into the target.

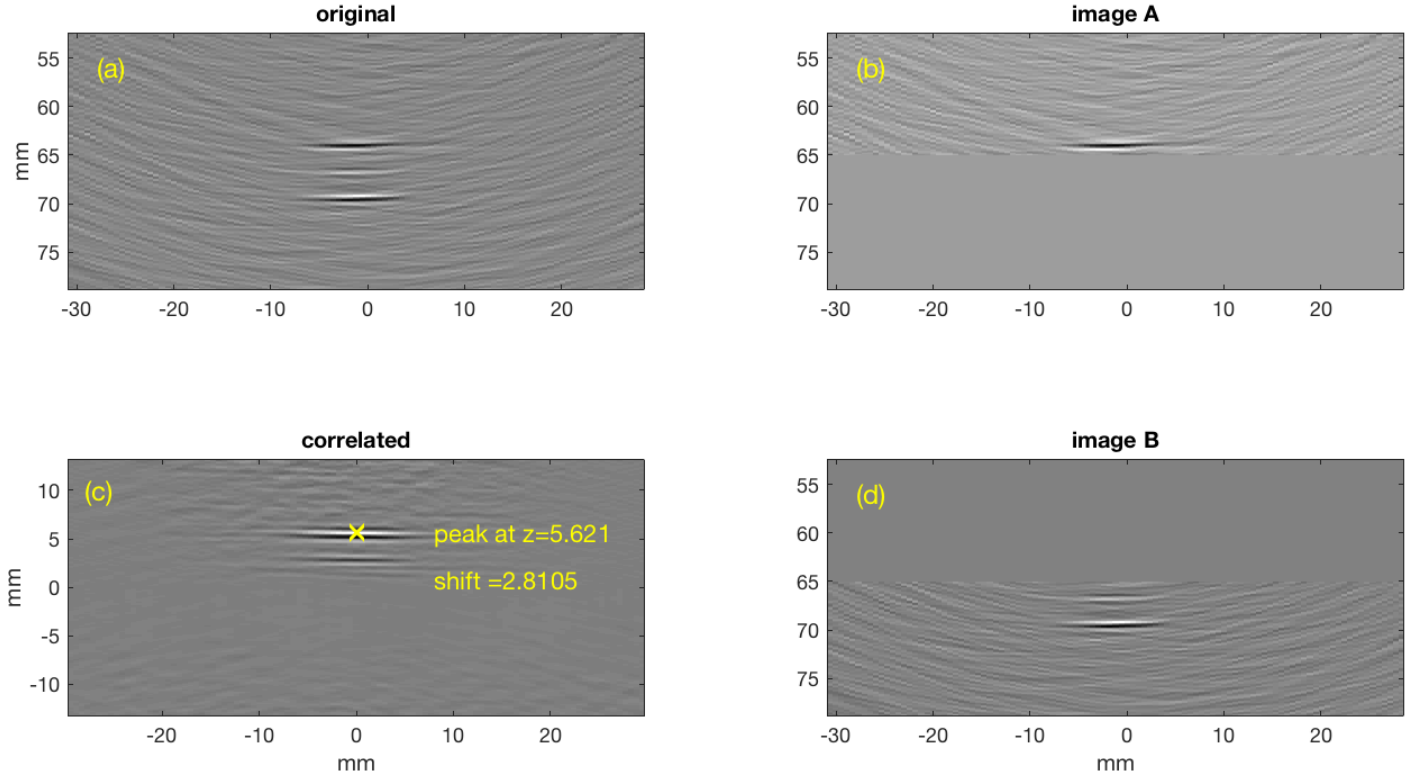

B. Additional Results

a. 4He into oil only, no scatterers with $v_s = 1540\ m/s$

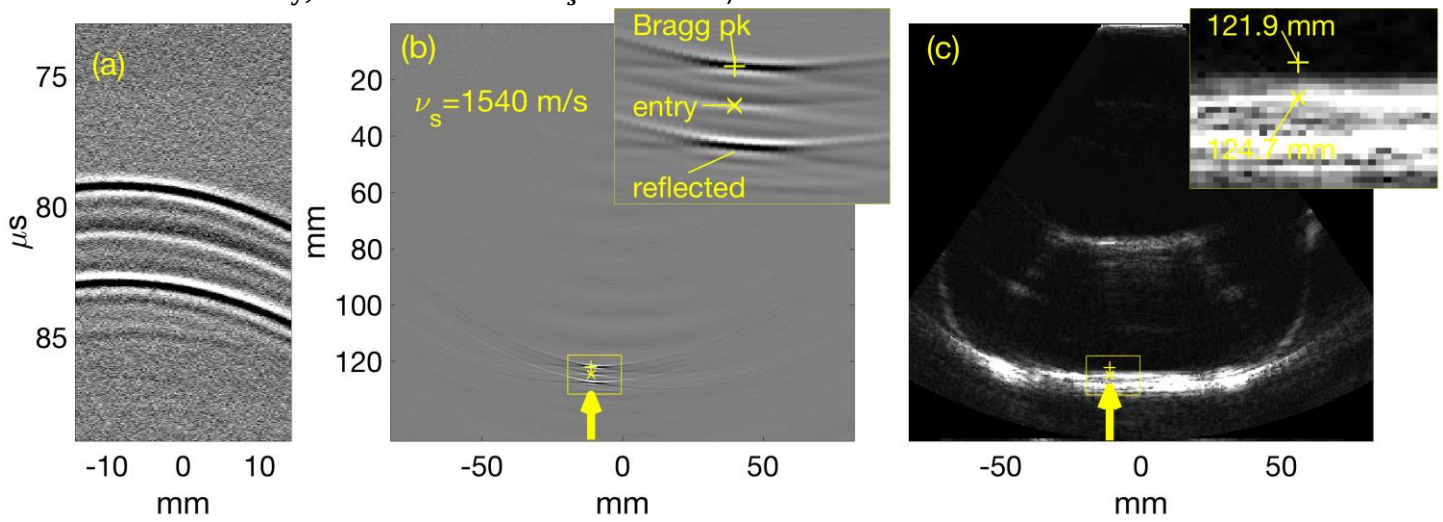

b. Bragg peak in bone w/gelatin (diffuse scatterer) with $v_s = 1470\ m/s$ and $v_s = 1620\ m/s$. Water background.

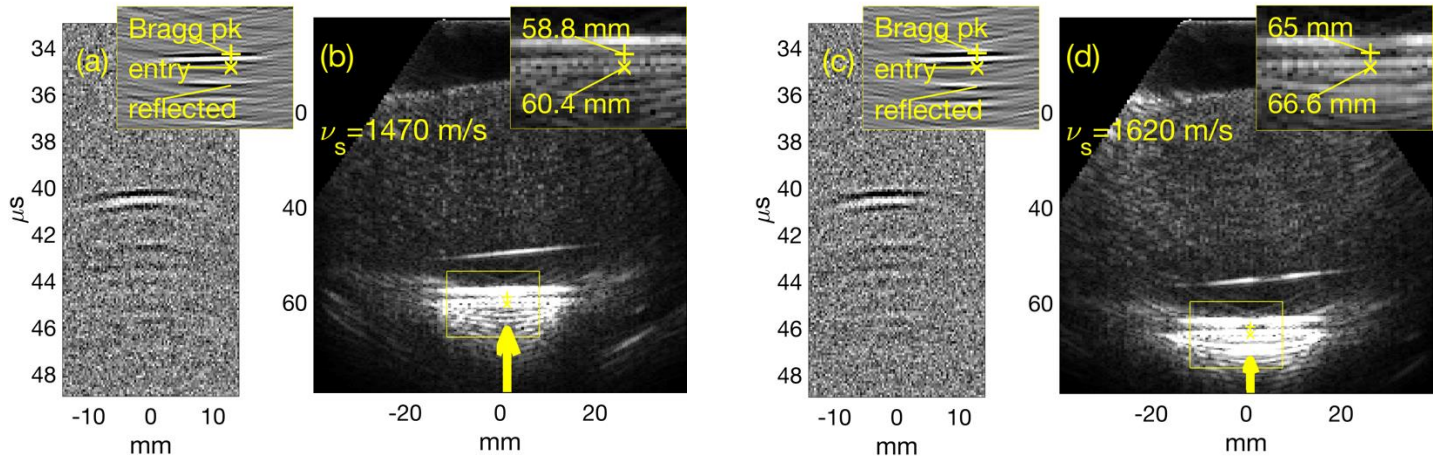

c. Protons into waterbath without bone, $v_s = 1470\ m/s\ \ and\ 1620\ m/s$.